

glaciology and perhaps also in studies of electrical conduction in ice.

Acknowledgment. I thank especially Dr. Michael Herron, who kindly supplied me with the anion data in Figure 1, and Prof. Dr. Chester C. Langway, Jr. for his encouragement and help during part of the study—both

at the Department of Geological Sciences, University of New York at Buffalo. Thanks also to the Commission for Scientific Research in Greenland, who funded the study. The Danish Natural Science Research Council funded my travel and participation in the Rolla symposium.

Registry No. Water, 7732-18-5.

Pressure Sintering of Ice and Its Implication to the Densification of Snow at Polar Glaciers and Ice Sheets

Norikazu Maeno* and Takao Ebinuma

The Institute of Low Temperature Science, Hokkaido University, N-19, W-8, Kita-ku, Sapporo, Japan 060 (Received: August 23, 1982; In Final Form: December 3, 1982)

During the sintering of an aggregate of ice particles, six or more different mechanisms contribute simultaneously to the growth of necks formed between the particles. This paper reviews briefly the works on ice sintering carried out so far and discusses the discrepancies among them with reference to the pressureless sintering diagrams which show fields of dominance for each mechanism under a given physical condition. The vapor transport mechanism was concluded to be dominant in most natural and laboratory conditions, but in the very initial stage surface diffusion is also an important mechanism. Densification of natural snow can be interpreted adequately by regarding it a phenomenon of pressure sintering or hot pressing, which is driven not only by the excess surface free energy but also by the externally applied pressure. The construction of pressure sintering diagrams by taking into account of three diffusional and dislocation creep mechanisms has shown various useful applications to the study of snow densification at polar glaciers and in laboratory experiments of pressure sintering of ice compacts.

Introduction

When a powder compact is kept at temperatures below but not far from the melting point, necks form between the powder particles and the aggregate increases in density. Such a phenomenon, known as sintering in the fields of powder metallurgy and ceramics, has also been studied for ice and snow particles by a number of workers.¹⁻⁶ However, the interpretation of the results, especially that concerned with the principal mechanism, has widely varied; in the first half of the present paper the work on ice sintering is briefly reviewed and discussed with reference to sintering mechanism diagrams for pairs of ice spheres, which were constructed by calculating sintering rates produced by six mass-transport mechanisms working simultaneously.

The densification of snow is discussed in the latter half of the present paper, realizing that the process can be regarded as that of pressure sintering or hot pressing. The concept is based upon the idea that the sintering is driven both by an excess surface free energy and by externally applied pressures.

Pressureless Sintering of Ice Spheres

Studies of ice sintering were initiated by Kingery¹ who measured the rates of growth of necks formed between two ice spheres in contact as functions of time, temperature, and radius of the spheres. Similar experiments were conducted by Kuroiwa² and Hobbs and Mason.³ All the above authors were interested in determining the dominant

mechanisms playing a part in the sintering of ice spheres, and analyzed their data to obtain parameters p and q appearing in the following equation:

$$(x/r)^q = Cr^{-p}t \quad (1)$$

where r is the radius of the ice sphere, x is the radius of the neck, t is the time, C is a constant depending upon temperature, and p and q are numerical constants depending upon the working mechanism. By comparing the observed values of p and q (Table I) with those expected from Kuczynski's theory⁷ of sintering accepted in the field of powder metallurgy (surface diffusion, $p = 4$, $q = 7$; lattice diffusion, $p = 3$, $q = 5$; vapor transport, $p = 2$, $q = 3$), Kingery concluded that sintering of ice spheres proceeds mainly by surface diffusion; on the other hand, Kuroiwa concluded that lattice diffusion; is the principal mechanism at temperatures above -10°C , but at lower temperatures surface diffusion is dominant.

Hobbs and Mason³ claimed that both of the above conclusions were doubtful because, in Kingery's experiment, ice spheres were not contained in an ice-saturated enclosure, and the interpretation according to Kuroiwa's results required that the lattice diffusion coefficient of ice was three orders of magnitude greater than that measured by radioactive tracers. Hobbs and Mason reevaluated Kuczynski's theory for the vapor transport mechanism of sintering by taking into account that the mean free path of water molecules in air at atmospheric pressure is not large compared with the radius of the neck, and the growth rate of the neck is controlled not only by the rate of arrival of molecules but also by the rate at which the latent heat of sublimation escapes by conduction through the air. Their conclusion based on their theory and measurements

(1) W. D. Kingery, *J. Appl. Phys.*, **31**, 833 (1960).

(2) D. Kuroiwa, *Tellus*, **13**, 252 (1961).

(3) P. B. Hobbs and B. J. Mason, *Phil. Mag.*, **9**, 181 (1964).

(4) P. V. Hobbs and L. F. Radke, *J. Glaciol.*, **6**, 879 (1967).

(5) R. Ramseier and C. M. Keeler, *J. Glaciol.*, **6**, 421 (1966).

(6) H. H. G. Jellinek and S. H. Ibrahim, *J. Colloid Interface Sci.*, **25**, 245 (1967).

(7) G. C. Kuczynski, *J. Met.*, **1**, 169 (1949).

TABLE I: Sintering Experiments for Two Ice Spheres in Contact

workers	radius, μm	temp, $^{\circ}\text{C}$	x/r	p	q
Kingery ^a	100-3000	-2.2 to -25.1	0.01-0.4	~ 4	6.1-7.1
Kuroiwa ^b	20-500	-2 to -20	0.08-0.5	~ 3	4.0-7.7
Hobbs and Mason ^c	15-350	-3 to -20	0.1-0.6	2.8-2.9	4.2-6.2

^a Reference 1. ^b Reference 2. ^c Reference 3.

was that the principal mechanism was vapor transport.

The discrepancies among the above conclusions by different authors could be attributed partly to the difference in temperature and particle radius (Table I) and to the accuracy in measurements: the size of the neck between the small ice spheres could only be measured relatively roughly with a microscope. However, the unique properties of ice sintering phenomena should also be taken into consideration: one is that ice sintering has usually been observed at high homologous temperatures (T/T_m is 0.9 or above), and the others are the high vapor pressures of ice, the occurrence of a surface phase change slightly below the melting point of ice, and so forth. Thus it might be naturally expected that several mechanisms work together in an ice sintering phenomenon.

Such a complex sintering phenomenon can be adequately studied by constructing sintering mechanism diagrams, which were first shown by Ashby⁸ and Swinkels and Ashby⁹ to be very useful in alloys and ceramics. These diagrams were constructed for pairs of ice spheres in contact, and we call them pressureless sintering diagrams to distinguish them from diagrams to be discussed in the following section. In the calculation six mass-transport mechanisms were assumed to work simultaneously and independently; rate equations for each of the mechanisms are as follows (for meaning of the symbols, refer to Figure 1 and Tables II and III):

1. surface diffusion from a surface source⁷

$$\left(\frac{\dot{x}}{r}\right)_1 = \frac{2\gamma_i\delta_s\Omega D_s K_1^3}{krT} \quad (2)$$

2. lattice diffusion from a surface source⁷

$$\left(\frac{\dot{x}}{r}\right)_2 = \frac{2\gamma_i\Omega D_l K_1^2}{krT} \quad (3)$$

3. vapor transport from a surface source³

$$\left(\frac{\dot{x}}{r}\right)_3 = \frac{\gamma_i\Omega K_1^2}{\rho_i k r T \left(\frac{kT}{D_v M p_v} + \frac{L_s^2 M}{k K T^2} \right)} \quad (4)$$

4. boundary diffusion from a grain boundary source¹⁰

$$\left(\frac{\dot{x}}{r}\right)_4 = \frac{4\gamma_i\delta_b\Omega D_b K_2^2}{krxT} \quad (5)$$

5. lattice diffusion from a grain boundary source⁸

$$\left(\frac{\dot{x}}{r}\right)_5 = \frac{4\gamma_i\Omega D_l K_2^2}{krT} \quad (6)$$

6. lattice diffusion from dislocation sources⁸

$$\left(\frac{\dot{x}}{r}\right)_6 = \frac{4\gamma_i\Omega x^2 D_l N}{9krT} \left(K_2 - \frac{3\mu x}{2\gamma_i r} \right) \quad (7)$$

Mass transport from a surface source to the neck (mechanisms 1-3) is driven by a curvature difference, $(1/a$

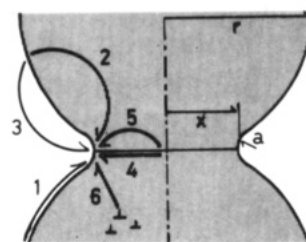


Figure 1. Six mechanisms by which mass is transported to the neck between two particles. Numbers correspond to the mechanisms listed in Table II. r and x are the radii of the particles and the neck respectively. a is the radius of curvature at the neck.

TABLE II: Mechanisms of Sintering

mechanisms	source of matter
1. surface diffusion	surface
2. lattice diffusion	surface
3. vapor transport	surface
4. boundary diffusion	grain boundary
5. lattice diffusion	grain boundary
6. lattice diffusion	dislocations

$-1/x) + 2/r$. The radius of curvature of the neck (a) can be approximated⁷ as $x^2/2(r-x)$, and by requiring that the driving force becomes zero at $x = r$, the curvature differences is expressed as⁸

$$K_1 = \left(\frac{1}{a} - \frac{1}{x} + \frac{2}{r} \right) \left(1 - \frac{x}{r} \right) \quad (8)$$

The curvature difference, which drives the mass transport from a grain boundary source (mechanisms 4 and 5) or from dislocation sources (mechanism 6), is

$$K_2 = \frac{1}{a} - \frac{1}{x} \quad (9)$$

The difference between K_1 and K_2 is small but becomes conceivable when x approaches r .

The meaning and numerical values of the symbols in the above equations are listed in Table III, but some explanations should be given. For the surface diffusion mechanism the appearance of a quasi-liquid layer or transition layer on an ice surface near the melting point was taken into account; it was assumed that $\delta_s D_s$, the product of the effective surface thickness and surface diffusion coefficient, is the sum of contributions associated with the intrinsic ice surface and the quasi-liquid layer:

$$\delta_s D_s = \delta_{is} D_{is} + \delta_{qll} D_{qll} \quad (10)$$

Here the intrinsic ice surface means one which is not covered with a quasi-liquid layer. In the calculation the intrinsic surface diffusion coefficient, D_{is} , was assumed to be equal to the boundary diffusion coefficient, D_b :

$$D_{is} = D_b = 3.0 \times 10^{-2} \exp(-E_b/kT) \text{ m}^2/\text{s} \quad (11)$$

where the activation energy for boundary diffusion, E_b , was set equal to two-thirds of that for lattice diffusion, E_l , which is 66.2 kJ/mol.¹¹ δ_{is} was set equal to 0.45 nm.

The diffusion associated with the quasi-liquid layer was considered as that through a thin supercooled water film;

(8) M. F. Ashby, *Acta Metall.*, **22**, 275 (1974).

(9) F. B. Swinkels and M. F. Ashby, *Acta Metall.*, **29**, 259 (1981).

(10) D. L. Johnson, *J. Appl. Phys.*, **40**, 192 (1969).

(11) K. Itagaki, *J. Phys. Soc. Jpn.*, **19**, 1081 (1964).

TABLE III: Symbols and Physical Data

a	radius of curvature at the neck
B	preexponential for power law of ice creep (eq 23): $B = 1.68 \times 10^{17} \text{ s}^{-1} (\text{MN/m}^2)^{-n}$ (-2 to -8 °C), 9.72×10^7 (-8 to -45 °C) ⁴¹
b	Burgers vector ($b = 0.45 \text{ nm}$)
c	radius of intermolecular interaction field ($c = 0.15 \text{ nm}$) ¹⁶
D_b	grain boundary diffusion coefficient of ice (eq 11)
D_l	lattice diffusion coefficient of ice ($D_l = 0.03 \exp(-E_l/kT) \text{ m}^2/\text{s}$) ¹¹
D_s	surface diffusion coefficient of ice (eq 10)
D_v	diffusion coefficient of water vapor in air at atmospheric pressure ($D_v = 1.199 \times 10^{-2} T^{1.75} \text{ m}^2/\text{s}$) ⁴²
d	radius of pores
δ_b	width of grain boundary ($\delta_b = 2b$)
δ_s	effective thickness of ice surface
E_b, E_l	activation energies for boundary and lattice diffusions ($E_b = (2/3)E_l$, $E_l = 66.2 \text{ kJ/mol}$) ¹¹
E_c	activation energy for steady-state creep of polycrystalline ice (eq 23): $E_c = 121.4 \text{ kJ/mol}$ (-2 to -8 °C), 74.5 (-8 to -45 °C) ⁴¹
$\dot{\epsilon}$	strain rate of densification ($\dot{\epsilon} = \dot{\rho}/\rho$)
γ_i	surface free energy of ice ($\gamma_i = 0.1 \text{ J/m}^2$)
$\Delta\gamma$	wettability parameter (eq 14)
K	thermal conductivity of air at atmospheric pressure ($K = 1.968 \times 10^{-3} T^{3/2}/(T + 125) \text{ J/K ms}$) ⁴²
K_1, K_2	curvature differences to drive sintering (eq 8 and 9)
k	Boltzmann constant ($k = 1.38 \times 10^{-23} \text{ J/K}$)
L_m, L_s	latent heats of melting and sublimation of ice ($L_m = 335 \text{ kJ/kg}$, $L_s = 2.85 \text{ MJ/kg}$)
m	mass of an H_2O molecule ($m = 2.989 \times 10^{-26} \text{ kg}$)
N	dislocation density
n	stress exponent (eq 23): $n = 3.16$ (-2 to -8 °C), 3.08 (-8 to -45 °C) ⁴¹
p_c	initial internal air pressure within pores at close-off
p_v	saturation pressure of water vapor over ice ($\log p_v = -2.4455646 \times 10^3/T + 8.2312 \log T - 1.677006 \times 10^{-2}T + 1.20514 \times 10^{-5}T^2 - 6.757169$, p_v in $(1/133.322) \text{ Pa} = \text{mmHg}$) ⁴²
r, \dot{r}	radius of particle and its time derivative
$\rho, \dot{\rho}$	bulk density of ice compact, that is snow, and its time derivative
ρ_i	theoretical density of ice ($\rho_i = 917 \text{ kg/m}^3$)
ρ_r	relative density ($\rho_r = \rho/\rho_i$)
ρ_{rc}	relative close-off density
Ω	volume of an H_2O molecule ($\Omega = 3.27 \times 10^{-29} \text{ m}^3$)
t	time
T	absolute temperature in Kelvin (K)
T_m	melting point of ice ($T_m = 273.15 \text{ K}$)
x, \dot{x}	radius of disk of contact between two particles, and its time derivative
μ	rigidity of ice ($\mu = 2.98 \times 10^9 \text{ Pa}$)

for the diffusion coefficient of the film we used the self-diffusion coefficient experimentally obtained by Pruppacher¹² for supercooled water in a temperature range from 0 to -20 °C, and fitted the data by the least-squares method to an accuracy of 3% as

$$\log D_{\text{qll}} = 2.0342 \times 10^{-2}T - 14.48 \quad (12)$$

(12) H. R. Pruppacher, *J. Chem. Phys.*, **56**, 101 (1972).

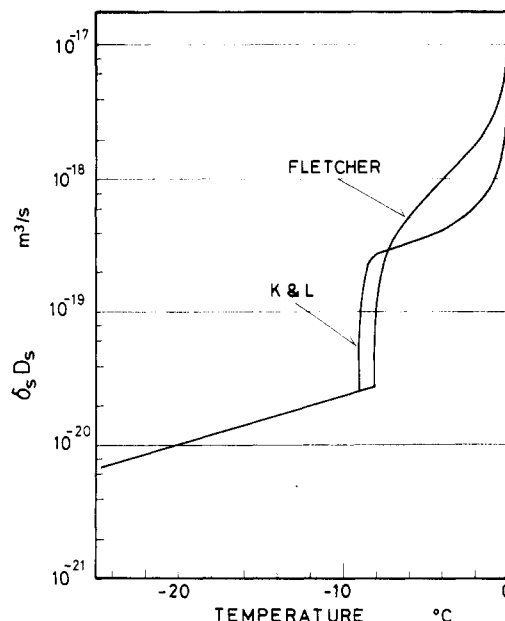


Figure 2. Temperature dependence of $\delta_s D_s$. Two curves were calculated by setting $Q = 2.5 \text{ nm}$ in eq 13 and $\Delta\gamma = 20 \text{ mJ/m}^2$ in eq 14.

where the units of D_{qll} and temperature (T) are m^2/s and K, respectively.

The effective thickness of a quasi-liquid layer, δ_{qll} , can be estimated from semiquantitative theories.¹³⁻¹⁶ Fletcher¹⁷ expressed his theoretical conclusion as

$$\delta_{\text{qll}} = Q - 2.5 \log (T_m - T) \text{ nm} \quad (13)$$

where Q is a constant ranging from 2 to 5 nm depending upon the physical parameters chosen. Kuroda and Lacmann,¹⁶ reevaluating the result of Lacmann and Stranski,¹⁵ obtained

$$\delta_{\text{qll}} = \left\{ \frac{2c^2 \Delta\gamma \Omega T_m}{L_m (T_m - T)} \right\}^{1/3} - c \quad (14)$$

where c is the radius of the intermolecular interaction field (set equal to 0.15 nm), L_m is the latent heat of fusion, and $\Delta\gamma$ is the wettability defined as a differential surface free energy:

$$\Delta\gamma = \gamma_i - (\gamma_w + \gamma_{i/w}) \quad (15)$$

where i and w mean ice and water, respectively. The critical temperature at which a quasi-liquid layer appeared was defined so that δ_{qll} estimated from eq 13 or 14 was equal to the thickness of a monolayer, namely, roughly 0.3 nm. Temperature dependences of $\delta_s D_s$ were calculated and plotted in Figure 2 for $Q = 2.5 \text{ nm}$ in eq 13 and $\Delta\gamma = 20 \text{ mJ/m}^2$ in eq 14; the above two equations with the two parameters imply that the surface phase change occurs at critical temperatures of -7.5 and -9.0 °C, respectively. In the calculation the former estimate was adopted simply because the unique property of ice was more apparent.

Figure 3 gives a pressureless sintering diagram for a pair of ice spheres of 35- μm radius. A similar diagram was constructed for ice particles of 350- μm radius, too. These radii were chosen by taking into account the experiments carried out so far (Table I). In principle the diagram shows

(13) N. H. Fletcher, *Phil. Mag.*, **7**, 255 (1962).

(14) N. H. Fletcher, *Phil. Mag.*, **18**, 1287 (1968).

(15) R. Lacmann and I. N. Stranski, *J. Cryst. Growth*, **13/14**, 236 (1972).

(16) T. Kuroda and R. Lacmann, *J. Cryst. Growth*, **56**, 189 (1982).

(17) N. H. Fletcher in "Physics and Chemistry of Ice", E. Whalley et al., Ed., Royal Society of Canada, Ottawa, 1973, p 132.

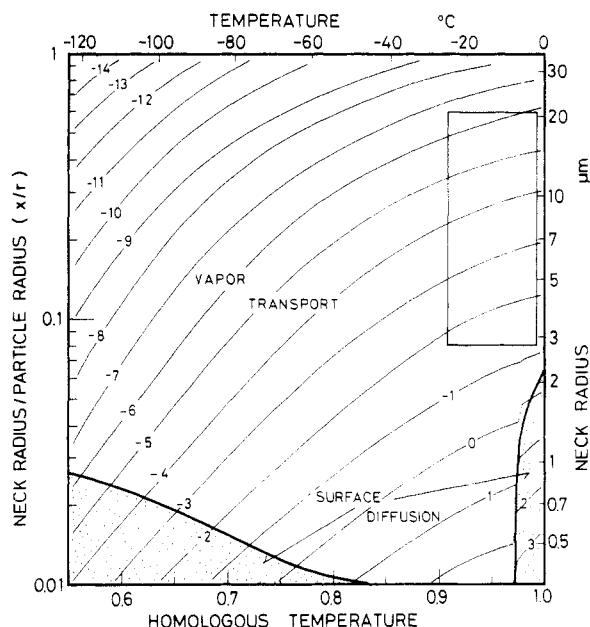


Figure 3. Pressureless sintering diagram for a pair of ice particles of 35- μm radius. On thick lines the normalized rates of neck growth due to the adjacent mechanisms are identical. Thin lines are contours of constant total normalized rate of neck growth (s^{-1}), the log of which is given as numerals. The box shows the range of ice sintering experiments carried out so far.

field of dominance of each of six mechanisms which contribute to the sintering, and the rate of neck growth or extent of sintering that all the mechanisms, acting together, produce. The axes are normalized neck radius (x/r) and homologous temperature (T/T_m). Within each of fields divided by thick lines a single sintering mechanism is dominant; on the lines rates of neck growth due to the adjacent mechanisms are identical. Thin lines superimposed on the fields are contours of constant total sintering rate, that is the sum of normalized rates of neck growth due to the six mechanisms:

$$\left(\frac{\dot{x}}{r}\right)_{\text{total}} = \sum_{i=1}^6 \left(\frac{\dot{x}}{r}\right)_i \quad (16)$$

The diagram in Figure 3 is characterized by a large field of mechanism 3 (vapor transport) and by the apparent effect of the surface phase change near the melting point. The former effect can be attributed to the high vapor pressure of ice as compared with other materials. For instance the homologous temperatures at which the vapor pressure of a material is 133.3 Pa (≈ 1 mmHg) are 0.94 for ice, 1.67 for Al, 0.64 for CO_2 , 1.40 for Cu, 1.32 for Ag, and 1.06 for NaCl; except for ice and CO_2 the vapor pressure can be such a meaningful value for sintering only above the melting point.

The latter effect, caused by the appearance of the quasi-liquid layer, is a unique property of ice. According to the diagram the surface diffusion mechanism is dominant at smaller neck sizes, and it is apparent from eq 2 that the field of surface diffusion extends to larger neck sizes as the particle radius decreases. It should be mentioned, however, that the enhanced mass transport by the mobility of water molecules in the quasi-liquid layer can also be interpreted as viscous flow instead of surface diffusion.⁶

Compared with others, contributions from lattice diffusion from dislocation sources (mechanism 6) are negligibly small even near the melting point and at dislocation densities as high as 10^{10} m^{-2} . Mechanisms 2, 4, and 5 are important contributors though they are not dominant mechanisms. Figure 4 gives the normalized growth rate

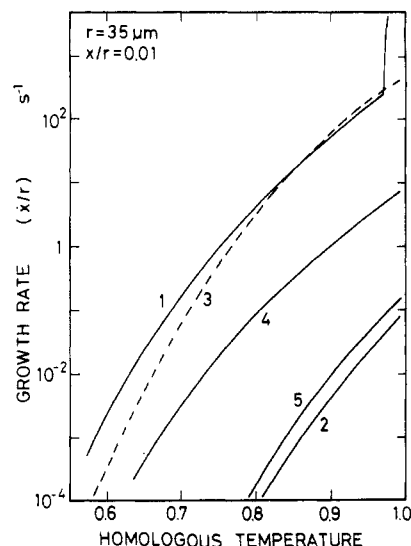


Figure 4. Temperature dependence of the normalized rates of neck growth due to each mechanism when $x/r = 0.01$. The particle radius is 35 μm . Numerals indicate mechanisms in Table II.

of each mechanism when $x/r = 0.01$. The contributions from mechanisms 2, 4, and 5 are small but not negligible; it can be expected that the changes in the structures of ice particles including grain boundaries and air bubbles might be caused by the mass flow by these mechanisms as reported by Kuroiwa.²

In Figure 3 the rectangular region implies the range of measurements carried out so far. The data lie in a field in which vapor transport is dominant. However, the proximity of the small neck-size end to the surface diffusion-controlled field suggests that the contribution from it is also appreciable. The pressureless sintering diagram for a pair of ice spheres of 350- μm radius was also constructed, but its feature was the same as that shown in Figure 3 though the vapor transport field was even wider. It is apparent from the above discussion that the determination of a dominant mechanism solely on the basis of observed values of p and q is misleading because the sintering rate is usually the sum of contributions from several mechanisms.

Stages of Snow Densification and Pressure Sintering of Ice

In practice the sintering of ice compacts or snow is by far more important than that of two ice spheres in contact. The densification of seasonal snow in northern countries and the transformation of snow into ice at polar glaciers and ice sheets are accomplished through sintering processes. In these cases, however, the sintering process is driven not only by the excess surface free energies in the system but also by externally applied pressures.

The densification process of snow at polar glaciers has been divided into three stages by two critical densities:¹⁸⁻²⁰ snow deposits densify first by mechanical destruction and packing of snow particles till the first critical density of 550 kg/m^3 (relative density $\rho_r = 0.60$), second by plastic deformation and recrystallization till the second critical density of 820–840 kg/m^3 ($\rho_r = 0.89$ – 0.92), and finally by the shrinkage of entrapped air bubbles until the theoretical density of ice (917 kg/m^3) is attained. Anderson and

(18) M. Perutz and G. Seligman, *Proc. R. Soc. London, Ser. A*, **172**, 335 (1939).

(19) D. L. Anderson and C. S. Benson in "Ice and Snow, Properties, Processes and Applications", W. D. Kingery, Ed., M.I.T. Press, Boston, 1963, p 391.

(20) C. S. Benson, SIPRE Research Report 70, 1962, p 1.

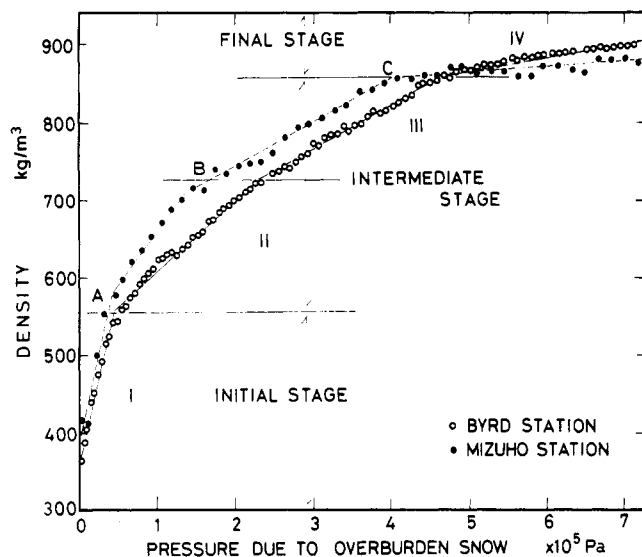


Figure 5. Density-pressure relationships at Byrd and Mizuho Stations in Antarctica. The pressure is the load due to the overburden snow, which can be converted to time by division by the accumulation rate of snow, namely, 157 kg/(m² year) at Byrd Station³⁸ and 70 kg/(m² year) at Mizuho Station.³⁹ A, B, and C show the three critical densities, and the stages, I, II, III, and IV of snow densification, and the initial, intermediate, and final stages of pressure sintering are also shown. Density data used are given in Gow³⁸ and Narita and Maeno.⁴⁰

Benson¹⁹ explained the first critical density to correspond to a maximum packing density which could be attained with granular aggregates. At the second critical density intercommunicating air channels are pinched off and entrapped as independent bubbles in ice.

The existence of an additional critical density of 730 kg/m³ ($\rho_r = 0.80$) was suggested by Maeno^{22,23} on the basis of electrical and other physical analyses of Antarctic snow cores: at that density, the bonding and packing mode of constituent snow particles reaches an optimum state, that is, the contact between particles becomes maximum and air bubbles are only included as thin cylinders along the intersections of several grain boundaries. It may be postulated²⁴ that the shapes of the particles at this state should correspond to those of equilibrium space-filling polyhedrons of the type of Kelvin's²⁵ or Williams'²⁶ tetrakaidecahedron.

Figure 5 gives typical relationships between the snow density and pressure due to the overburden snow at Byrd and Mizuho Stations in Antarctica. Though the two curves do not coincide with each other because of the difference in the temperature and accumulation rate of snow, three critical densities, A, B, and C, in the figure, can be clearly identified, which divide the densification process into four stages, I – IV; a detailed discussion of each of the stages is reported elsewhere.²⁷

In powder metallurgy and ceramics, the densification process through pressure sintering has been divided into three stages;²⁸ in the initial stage the rearrangement and fracture of particles occur first, and necks formed between particles grow rapidly by diffusion and plastic flow. This stage is followed by an intermediate stage in which the

necks are now fairly large and most of pores are cylindrical and connected to each other. The densification proceeds by the shrinkage of these cylinders in radius. By the time the final stage is reached, the cylindrical pores become unstable and are pinched off to form closed spherical pores. Further densification is caused by the same mechanisms as in the intermediate stage.

It can be supposed that the initial, intermediate, and final stages of pressure sintering correspond to stages I, II/III, and IV in snow densification, respectively.

Pressure Sintering Diagrams of Ice

The process of pressure sintering is more complicated than that of normal sintering under a pressureless condition: comprehensive literature reviews^{29,30} show that the kinetics and mechanisms of pressure sintering can be interpreted by analogy with creep kinetics developed for polycrystalline materials and with appropriate modifications for driving forces. It has also been recognized that more than one process, either in series or parallel, are simultaneously operating, including diffusional creep, dislocation creep, grain boundary sliding, and so forth.

Wilkinson and Ashby³¹ have attempted to clarify the complex picture by the use of pressure sintering diagrams, which, like the diagrams for pressureless sintering as discussed earlier, give a regime of dominance of each mechanism. We have constructed similar diagrams for compacts of identical ice spheres in the intermediate and final stages of pressure sintering; the initial stage was not included in the diagrams because densification takes place together with the growth of necks between ice particles, and adequate formulations for the process have not been obtained yet. It is assumed that densification in the latter two stages occurs by diffusional creep and plastic flow mechanisms. The diffusion creep models presented by Coble³² were adopted in the calculation, according to which the strain rate of densification of a powder compact, $\dot{\epsilon}$, in the intermediate stage is given as

$$\dot{\epsilon} = \dot{\rho}/\rho = \frac{10D_l\Omega}{3kr^2T} \left(\frac{\tau}{\rho_r} + \frac{\gamma_i}{d} \right) \quad (17)$$

for lattice diffusion, and

$$\dot{\epsilon} = \frac{37\delta_b D_b \Omega}{2kr^3T} \left(\frac{\tau}{\rho_r} + \frac{\gamma_i}{d} \right) \quad (18)$$

for grain boundary diffusion. Here τ is the applied stress, d is the radius of the pores, and the other symbols are the same as before (Table III). Equations 17 and 18 are essentially the Nabarro–Herring and Coble equations, respectively, which are often applied to the study of the creep behavior of polycrystalline materials. However, in the driving force the contribution from surface energy is included and an effective stress in porous mass, τ/ρ_r , is adopted instead of τ .

In the final stage eq 17 cannot describe adequately the kinetics, and the following equation³² was used:

$$\dot{\epsilon} = \frac{3D_l\Omega}{\rho_r k r^3 T} \frac{dr}{r-d} \left(\frac{\tau}{\rho_r} + \frac{2\gamma_i}{d} \right) \quad (19)$$

where d is now the radius of the spherical pores. For boundary diffusion the surface energy term in eq 18 was

(21) C. C. Langway, SIPRE Research Report 77, 1967, p 1.

(22) N. Maeno, *Mem. Natl. Inst. Polar Res.*, 10, 77 (1978).

(23) N. Maeno, H. Narita, and K. Araoka, *Mem. Natl. Inst. Polar Res.*, 10, 62 (1978).

(24) N. Maeno, "Kohri no Kagaku" (The Ice Science), Hokkaido University Press, Sapporo, 1981, p 158.

(25) W. T. Kelvin, *Phil. Mag.*, 24, 503 (1887).

(26) R. E. Williams, *Science*, 161, 276 (1968).

(27) N. Maeno, *Mem. Natl. Inst. Polar Res.*, 24, 204 (1982).

(28) R. L. Coble in "Sintering and Related Phenomena", G. C. Kuczynski et al., Ed., Gordon and Breach, New York, 1967, p 329.

(29) R. L. Coble in "Sintering and Related Phenomena", G. C. Kuczynski, Ed., Plenum Press, New York, 1973, p 177.

(30) R. M. Springs and S. K. Dutta in "Sintering and Related Phenomena", G. C. Kuczynski, Ed., Plenum Press, New York, 1973, p 369.

(31) D. S. Wilkinson and M. F. Ashby, *Sci. Sintering*, 10, 67 (1978).

(32) R. L. Coble, *J. Appl. Phys.*, 41, 4798 (1970).

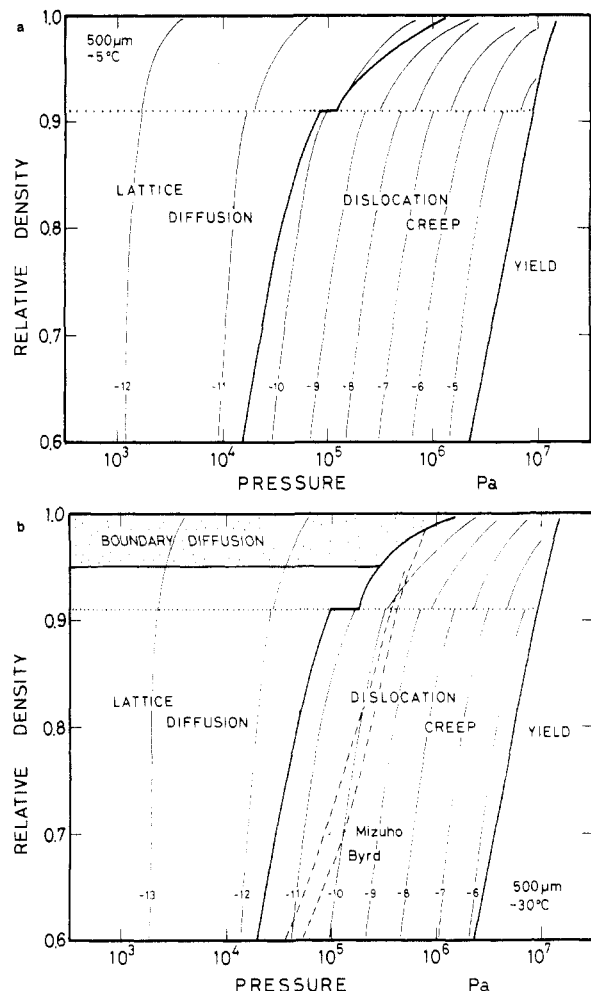


Figure 6. Pressure sintering diagrams for ice particles of 500- μm radius at temperatures of -5 (a) and -30 $^{\circ}\text{C}$ (b). The strain rates of densification due to adjacent mechanisms are identical on thick lines. Thin lines are contours of constant total strain rate of densification (s^{-1}), the log of which is given as numerals. Dotted lines indicate the transition from the intermediate to final stages. The dashed lines in (b) are the density-pressure profiles at Byrd and Mizuho Stations in Antarctica shown in Figure 5.

also replaced by $2\gamma_i/d$. d was estimated from the following mass-conservation relation:

$$\rho_r = 1 - (d/r)^3 \quad (20)$$

The densification rate due to plastic flow associated with dislocations was calculated on the basis of a model presented by Wilkinson and Ashby,³³ which was derived by considering pores as cylindrical or spherical holes surrounded by thick shells of solid material which flew by a power-law creep mechanism. The strain rate of densification was expressed as

$$\dot{\epsilon} = \frac{2A(1 - \rho_r)}{\{1 - (1 - \rho_r)^{1/n}\}^n} \left(\frac{2\tau}{n} \right)^n \quad (21)$$

in the intermediate stage, and

$$\dot{\epsilon} = \frac{3A(1 - \rho_r)}{2\{1 - (1 - \rho_r)^{1/n}\}^n} \left[\frac{3}{2n} \left\{ \tau - \frac{(1 - \rho_{rc})\rho_r}{(1 - \rho_r)\rho_{rc}} p_c \right\} \right]^n \quad (22)$$

in the final stage. Here A and n are constants appearing in the following empirical power law of creep:

$$\text{strain rate} = A\tau^n = B\tau^n \exp(-E_c/kT) \quad (23)$$

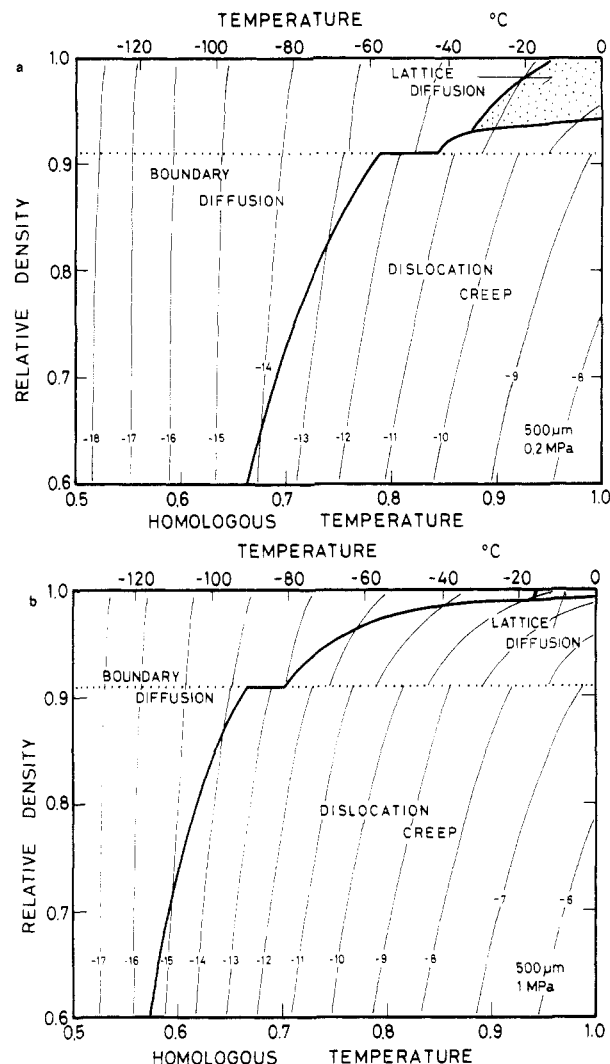


Figure 7. Pressure sintering diagrams for ice particles of 500- μm radius under pressures of 0.2 (a) and 1 MPa (b).

where B is a constant and E_c is the activation energy for creep. p_c is the initial internal air pressure within the pores when the pores are closed off in ice at a relative density of ρ_{rc} .

Pressure sintering diagrams for compacts of ice particles of 500- and 50- μm radii are shown in Figures 6–8. In the calculation the relative close-off density and air pressure were set equal to $\rho_{rc} = 0.91$ and $p_c = 0.1$ MPa (1 bar), respectively, other numerical values being as listed in Table III. The yield criterion was determined by the failure strength of polar snow, τ_f , measured by Kovacs et al.³⁴ at -25 $^{\circ}\text{C}$ under an unconfined compressive condition, which was well-fitted by the fourth degree polynomial

$$\tau_f = 1.43 \times 10^7 - 1.156 \times 10^5 \rho + 337.4 \rho^2 - 0.4174 \rho^3 + 2.049 \times 10^{-4} \rho^4 \quad (24)$$

where τ_f is expressed in Pa and ρ in kg/m^3 .

Parts a and b of Figure 6 are diagrams for ice particles (500- μm radius) pressure sintered at -5 and -30 $^{\circ}\text{C}$, respectively. The axes are relative density, ρ_r , and applied pressure, τ . The dotted lines at the relative density of 0.91 indicate the transition from the intermediate to the final stages. Sets of rate equations are changed appropriately in the calculation when the transition line is crossed. On the thick lines the strain rates of densification due to each

(33) D. S. Wilkinson and M. F. Ashby, *Acta Metall.*, **23**, 1277 (1975).

(34) A. Kovacs, W. F. Weeks, and F. Michitti, CRREL Research Report 276, 1969, p 1.

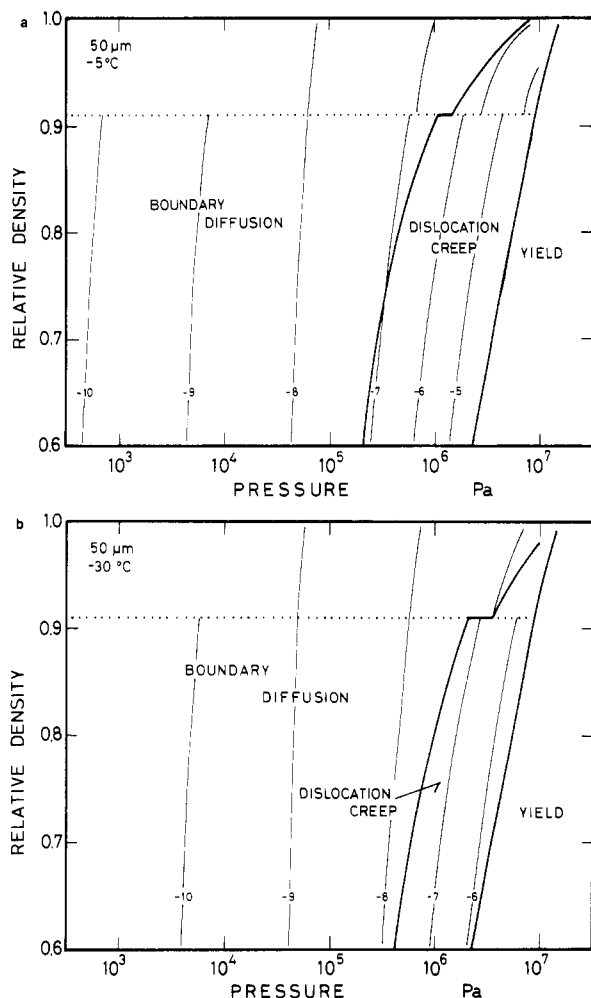


Figure 8. Pressure sintering diagrams for ice particles of 50- μm radius at temperatures of -5 (a) and -30 $^{\circ}\text{C}$ (b).

of the adjacent mechanisms are identical. Thin lines indicate total strain rate.

The diagrams show four different mechanism fields. At low pressures below about 10 kPa lattice and boundary diffusion creep mechanisms control the densification rate. Above 10 kPa plasticity becomes important and most of the densification is controlled by the dislocation creep mechanism, and above the failure strength, roughly 10 MPa, all the densification is caused by plastic yielding.

Parts a and b of Figure 7 are diagrams for the same compact at constant pressures of 0.2 and 1 MPa, respectively. The axes are now relative density and homologous temperature, T/T_m . It is reasonably shown that at 0.2 MPa (2 bar) the densification is controlled by dislocation creep at temperatures above about $0.7T_m$, but that diffusional creep mechanisms are predominant at lower temperatures and in the final stage. The decrease in the contribution from dislocation creep in the final stage is attributable to the increase in the air pressure within pores which results in a decrease in the effective stress. When the stress is increased to 1 MPa (Figure 7b) the region of the dislocation mechanism extends into that of lattice diffusion creep. It should be noted in Figures 6 and 7 that lattice diffusion creep is only dominant at temperatures near the melting point of ice.

An increase in the area of grain boundaries changes the diagram considerably. In the diagrams for ice particles of 50- μm radius, pressure sintered at -5 and -30 $^{\circ}\text{C}$ (parts a and b of Figure 8), lattice diffusion dominant regions do not appear, and the fields of boundary diffusion creep are

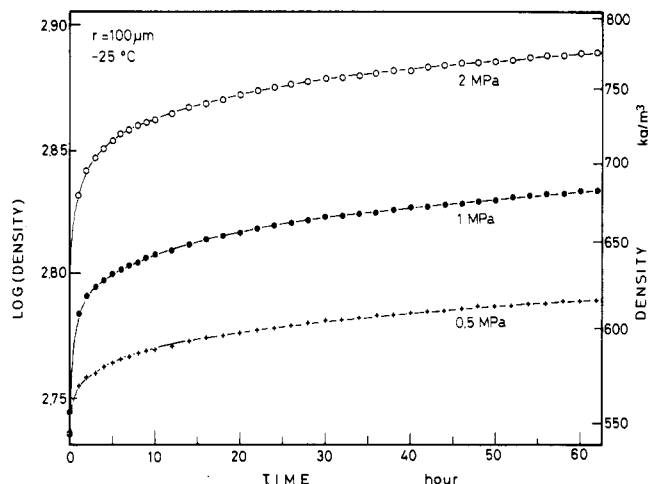


Figure 9. Experimentally measured density vs. time for a compact of ice particles of 100- μm radius, pressure sintered at -25 $^{\circ}\text{C}$ under various constant pressures.

much more broader as compared with those in Figure 6.

Discussion

Many diagrams of pressureless sintering for pairs of ice particles and of pressure sintering for ice compacts have been constructed and proved to be very useful to interpret the complicated mechanisms of ice sintering. The pressureless sintering diagrams showed distinct contributions from the vapor transport and surface diffusion mechanisms, both of which are closely associated with the unique properties of ice: high vapor pressures and active surface layers.

One of the important approximations made in constructing pressure sintering diagrams is related to the effective stress. It has long been recognized that the effective stress acting in a porous compact is much higher than the applied stress. We have applied Coble's estimate,³² τ/ρ_r . It should be noted, however, that this estimate is one of the most modest: the intensity factor, that is the ratio of the effective stress to the applied stress, is no more than 2 even at a relative density of 0.5. Rao and Chaklader³⁵ have estimated the intensity factor by assuming that the particles are monosized spheres with known packing geometry under a primarily uniaxial stress. They have shown that it is very much larger than that considered by previous workers; it is larger than 3 below 0.79 relative density for all the geometric models considered. It is therefore possible that the regimes of diffusional creep might be wider than those shown in the present paper if such intensity factors were used.

The density-pressure profiles of polar snow, already shown in Figure 5, are plotted again in the pressure sintering diagram in Figure 6b. The mean annual temperatures at the sites are -28 $^{\circ}\text{C}$ at Byrd Station and -33 $^{\circ}\text{C}$ at Mizuho Station, and the densification can be considered as an isothermal process. The figure shows that the densification at the two sites is caused primarily by the dislocation creep mechanism, and that the measured strain rates of densification, $(1-8) \times 10^{-11} \text{ s}^{-1}$ at the two sites,²⁷ are in reasonable agreement with those predicted. However, the possible extension and proximity of the diffusion creep fields suggest simultaneous contributions of lattice and boundary creep mechanisms.

Some preliminary results of pressure sintering experiments under way in our laboratory are shown in Figures

(35) A. S. Rao and A. C. D. Chaklader, *J. Am. Ceram. Soc.*, **55**, 596 (1972).

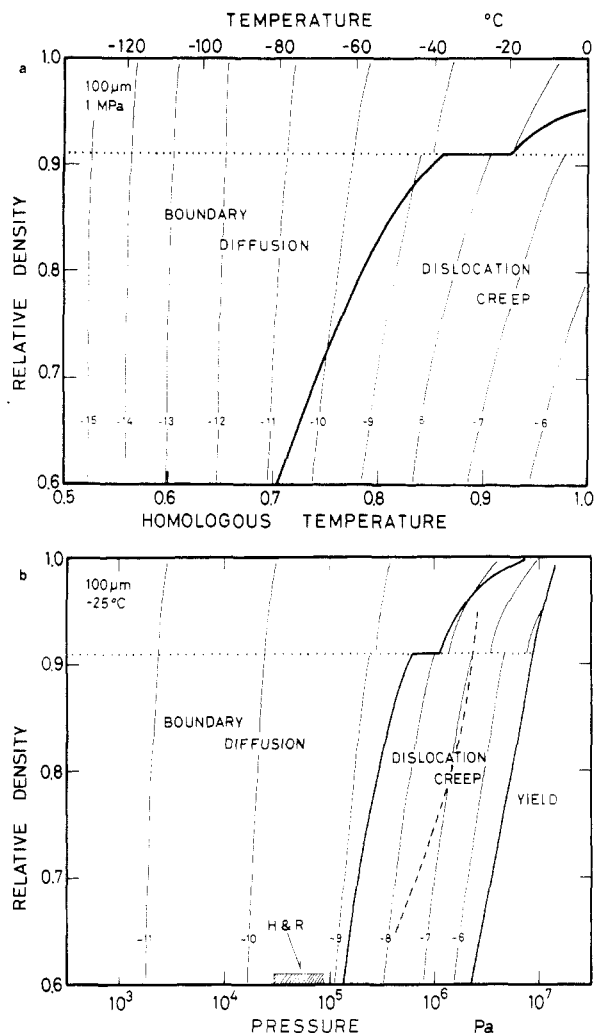


Figure 10. Pressure-sintering diagrams of ice particles of 100- μm radius under a pressure of 1 MPa (a) and at a temperature of -25°C (b). The dashed line in (b) shows the result shown in Figure 9, namely, the observed relative density and pressure at which the strain rate of densification is $1 \times 10^{-7} \text{ s}^{-1}$. The shaded area indicates the experimental range of Hobbs and Radke,⁴ particle radius ranging from 100 to 500 μm and temperature from -2.5 to -26.5°C .

9 and 10; Figure 9 gives density-time relations of compacts of ice spheres of 100- μm radius pressure sintered at -25°C under various stresses. From these curves strain rates of densification at given densities and stresses can be estimated; in Figure 10b relative density and stress at which the strain rate is 10^{-7} s^{-1} is plotted. The data again lie in

the dislocation creep field and agree roughly with the calculated contour. More details will be reported in the near future.

The range of experiments done by Hobbs and Radke⁴ is indicated in Figure 10b by a shaded box. They measured the change in volume of ice compacts (100–500- μm radius) contained in a balloon and immersed in a mercury reservoir at temperatures from -2.5 to -26.5°C and have reported that the densification was not affected by a hydrostatic overpressure caused by the mercury. However, the pressure is estimated to have amounted to 30–90 kPa, and so Figure 10b suggests that their experimental results might be more adequately interpreted by the boundary diffusion mechanism in pressure sintering. This conclusion is in accordance with their result that the effective lattice diffusion coefficient estimated from their experiments was about three orders of magnitude larger than that obtained from radioactive measurements if the lattice diffusion was assumed to be the only working mechanism.

It should be mentioned finally that the rate equations used in constructing the pressureless and pressure sintering diagrams include several approximations and idealizations, and that the numerical data for the physical properties of ice used are not necessarily reliable. Therefore the relative dominance of different mechanisms should be considered now as flexible one. Furthermore the sizes of the crystal grains were assumed constant in the calculation, but grain growth has frequently been reported during the densification process of snow;^{36,37} grain growth, possible distribution of grain sizes, geometric configurations, and also crystal boundaries within polycrystalline grains should be taken into account to improve the diagrams.

Acknowledgment. This work was partly supported by Grants-in-Aid for Research in Natural Disaster, Co-operative Research and Scientific Research of the Ministry of Education, Science and Culture, Japan, and by the National Institute of Polar Research.

Registry No. Water, 7732-18-5.

- (36) A. J. Gow, CRREL Research Report 300, 1971, p 1.
- (37) H. Narita and N. Maeno, *Antarct. Rec.*, **67**, 11 (1979).
- (38) A. G. Gow, CRREL Research Report 197, 1968, p 1.
- (39) N. Maeno and H. Narita, *Antarct. Rec.*, **67**, 18 (1979).
- (40) H. Narita and N. Maeno, *Mem. Natl. Inst. Polar Res.*, **10**, 136 (1978).
- (41) R. Barnes, D. Tabor, and J. C. F. Walker, *Proc. R. Soc. London, Ser. A*, **324**, 127 (1971).
- (42) E. W. Washburn, Ed., "International Critical Tables", McGraw-Hill, New York, 1929, Vol. IV and V.